Journal of the European Ceramic Society 39 (2019) 2091–2102

Contents lists available at ScienceDirect

Journal of the European Ceramic Society

journal homepage: www.elsevier.com/locate/jeurceramsoc

Mechanics-aided digital image correlation for the investigation of piezoelectric and ferroelectric behaviour of a soft PZT

Valentin Segouin*, Mathieu Domenjoud, Yves Bernard, Laurent Daniel

GeePs | Group of Electrical Engineering - Paris, CNRS, CentraleSupélec, Univ. Paris-Sud, Université Paris-Saclay, Sorbonne Université, 3 & 11 rue Joliot-Curie, Plateau de Moulon, 91192, Gif-sur-Yvette CEDEX, France

ARTICLE INFO

Keywords:
Hysteresis loops
Global DIC
Strain field
Regularisation
Strain homogeneity

ABSTRACT

The strain response of a polarised PZT was characterised using Digital Image Correlation (DIC). The DIC algorithm is based on a global approach and regularises the displacement field using the balance equations of solid mechanics. The measurement error is reduced by correcting the displacements that are mechanically not admissible. A ferroelectric test showed that the standard deviations of strain fields remain mostly under 1.2×10^{-4} for an element size of 64 px. The standard deviation on the average value is 3×10^{-6}. The strain field is homogeneous and its average value is consistent with the strain obtained from a CCD laser measurement device. The longitudinal strain, transverse strain and polarisation response of the PZT were measured for bipolar and unipolar loadings ranging from 50 to 5000 V/mm. Material properties were extracted from these measurements. This work shows the advantages of a novel 2D-DIC algorithm for piezoelectric strain characterisation.

1. Introduction

Piezoelectric and ferroelectric materials are increasingly used in various applications such as sensors [1–3], actuators [4], harvesting devices [5], converters [6], non-volatile memories [7], filters [8] and oscillators [9]. The performance and reliability of such devices depend on the material electromechanical properties, which consequently need to be characterised. In the past decades, such characterisation was largely developed and the piezoelectric, ferroelectric, ferroelastic and dielectric properties of ferroelectrics were the subject of numerous studies [10–17]. Yet, the test conditions are difficult to control due to the strong interplay between thermal, mechanical and dielectric properties. For example, stress and temperature induce strong variations of the piezoelectric coefficient d_{33} for a single ferroelectric crystal [18]. The electric field also contributes to significant variations in the dielectric and piezoelectric coefficients of $BaTiO_3$ and PZT ceramics [17]. It is then necessary to seek ways of revealing, at the macroscopic scale, the presence of anomalies such as inhomogeneous stress, electric field or temperature.

In the case of strain measurement, strain gauges [19] or linear variable displacement transducer (LVDT) [20] are classically used. Both techniques offer satisfying resolution and can furthermore be used under several types of external loadings [15,21]. However, it is not possible to obtain information on strain homogeneity with these techniques. Indeed, the minimum strain gauge size is limited to the millimetre which restricts the density of the measurement points. This issue also applies to LVDT. Another drawback is that only one direction can be measured per gauge grid or transducer. To measure the longitudinal and transverse strain simultaneously, another grid or transducer is needed. Such measurement devices are difficult to design, especially under coupled loadings or for ferroelectric films. Hence, the longitudinal strain is generally the only measured strain component [15,20–24] and the transverse strain is often discarded.

Digital Image Correlation (DIC) opens up opportunities for the measurement of strain on ferroelectric materials. This strain measurement technique is contactless, not scale-limited, allows 2D full-field measurements and is compatible with any imaging method. One requirement is that trackers or textures are needed in the images so as to observe displacements. DIC has already been used for classical mechanical experiments such as thermal [25], fatigue [26], ageing [27], high speed [28] or large strain [29] tests. Besides, active materials such as ferromagnetics [30,31], shape memory alloys [32,33] and piezoelectrics [34,35] were also studied. Regarding the piezoelectric studies [34,35], the DIC was dedicated to large strains and crack measurements. Recently, DIC was used to characterise the macroscopic ferroelectric behaviour of a 0.5 mm film [36] and to measure the piezoelectric coefficients of a piezoelectric wafer in the Rayleigh region [37]. In these works, the measurements were conducted in the air, with a

* Corresponding author.
E-mail address: valentin.segouin2@gmail.com (V. Segouin).

https://doi.org/10.1016/j.jeurceramsoc.2018.12.058
Received 2 October 2018; Accepted 28 December 2018
Available online 11 January 2019
0955-2219/

maximum electric field around 2 kV/mm and with the natural texture of the sample as DIC tracking pattern.

More recently, Chen and Kamlah improved the use of the DIC technique for ferroelectric [38] and ferroelastic [39] characterisations. The displacement and strain measurement errors were investigated and the notion of strain field homogeneity was introduced. Similarly to [37], DIC measurements were made using the natural texture of the sample. In the algorithm used, strains were obtained from a linear regression of the displacement field. Such a computation strategy drastically reduces the random part of the measurement error. For instance, for a regression over a distance of 1800 px and for static images, the strain error was about 10^{-6} while the local displacement error was 6.5×10^{-2} px. This strain error led the DIC measurement results to be in a good agreement with the LVDT technique in this case. However, such a strain computation process discards physical admissible results, for instance non-uniform strain components. A way to circumvent this problem while keeping a low uncertainty is to introduce a filter that takes into account mechanical admissibility of the solution. Recently, DIC has outperformed the displacement resolution of classical algorithms using such a filter [40]. The proposed algorithm, namely CorreliRT3, is able to compute displacements imposed during a mechanical test with a standard deviation under 10^{-2} px.

In this work, CorreliRT3 is used to characterise a ferroelectric sample from piezoelectric to ferroelectric strain levels. A speckle pattern is deposited on the sample to maximise the correlation quality. The correlation algorithm is described in a first part. The speckle deposition and the measurement device is detailed in a second part. The experimental error of the DIC setup is assessed with the help of a ferroelectric test on the PZT sample. Then, the strain of the PZT sample is measured under electric fields from piezoelectric to ferroelectric amplitudes. The piezoelectric coefficients, the susceptibility and the density of dissipated energy per cycle are extracted from this experiment. Their evolution as a function of the electric field amplitude is discussed in the last part. This work details in conclusion the potentialities, in terms of piezoelectric behaviour characterisation, of a DIC setup designed for high electric fields.

2. DIC technique

The Digital Image Correlation (DIC) technique was first introduced for 2D images by Sutton et al. [41]. This technique initially aims at measuring the full in-plane deformation of an object. For that purpose, two monochromatic images are obtained from this object (a reference picture and a deformed picture). Images are defined as 2D matrices where each value corresponds to a grey level amplitude. The matrices can be cropped to discard irrelevant data and in such cases, the remaining region is called Region Of Interest (ROI). The images or ROIs are then compared using a correlation algorithm. The algorithm initially proposed by Sutton et al. used a spatial 2D cross-correlation product. Under the hypothesis of grey level conservation, the cross-correlation product is maximum when the two images match. Thus, the displacement between images corresponds to the coordinates of the cross-correlation maximum. The computed displacement then refers to the mean displacement of the image centre. It is worth noting that for this algorithm, ROIs are rather divided in square subsets and the correlation is performed on each subset. It allows to define several displacement nodes hence a displacement field. This method is referred to as “local” (subset-based) DIC [41,42]. The displacement uncertainty of such algorithm is equal to one pixel since it is the numeric resolution of the image. However, interpolation methods were developed to improve the accuracy down to sub-pixel levels [43–45]. Since its first application, this DIC principle has been optimized. Measurement setups were improved and experimental errors minimised. A comprehensive state of the art review on these aspects can be found in [46].

Alternative computation techniques based on variational formulations were also developed. Such approaches are referred to as “global approaches”. In these algorithms, the correlation is computed over the whole image (or ROI) without sub-dividing it into subsets. It is then possible to insert, in the computation process, spatial regularisation techniques to constrain the displacement field and control its fluctuations [47,48]. Recently, a global approach based on a finite element description and on a mechanical regularisation has been developed and implemented [40,42]. It consists first in minimising iteratively the function Φ_c^2 related to difference of grey levels between two images:

$$\Phi_c^2 = \int_\Omega (f(x) - g[x + u(x)])^2 dx, \tag{1}$$

where:

Ω is the considered domain (subset in local approach, ROI in global approach).

f is the reference image.

g is the image in a deformed configuration.

x is the pixel coordinates.

$u(x)$ is the displacement of the pixel at coordinates x.

A Taylor expansion to the first order is made to linearize $g[x + u(x)]$ to $g(x) + \nabla f(x).\ u(x)$. Eq. (1) then leads to a linear system and it is possible to express this system in a matrix-vector product [42]:

$$[M]\{du\} = \{b\}, \tag{2}$$

where:

$[M]$ is a constant matrix representing the dyadic product of fields $\nabla f(x).\ \psi(x)$ where $\psi(x)$ is a chosen vector function constraining $u(x)$.

$\{b\}$ corresponds to the residual vector, weighted by $\nabla f(x)$. This quantity vanishes when a perfect match is obtained for each pixel.

This system is solved iteratively. An iteration consists first in computing $\{b\}$ from f and. Eq. (2) is then solved to find $\{du\}$ and the total displacement field $\{u\}$ is updated. Afterwards, the image g is corrected and a new iteration starts. The iterative process stops when $\{du\}$ reaches a quantity defined by the user. It is worth noting that, as a linearization is used to solve Eq. (1), the solution $\{u\}$ is defined only for small increments $\{du\}$.

In the program Correli RT3, the displacement field $u(x)$ is in addition constrained to fulfil mechanical admissibility of the solution. For that purpose, a linear-like elastic relation is imposed in a Finite Element sense:

$$[K]\{u\} = \{f\}, \tag{3}$$

where:

$[K]$ is the stiffness matrix.

$\{f\}$ is the nodal forces vector.

$\{u\}$ is the displacement field.

As this minimisation is computed in a Finite Element sense, the ROI is discretised using a mesh. Equations are solved for each node of this mesh. In the case of CorreliRT3, the mesh elements are chosen to be triangular (also called T3-element). Starting from Eq. (3), the mechanical residual function Φ_m^2 is introduced to regularise the displacement of all interior nodes:

$$\Phi_m^2 = \{u\}^t [K]^t [K]\{u\}, \tag{4}$$

The displacements at the edges of the mesh are regularised using an energy term based on the displacements at the mesh boundary:

$$\Phi_b^2 = \{u\}^t [L]^t [L]\{u\}, \tag{5}$$

where:

$[L]$ is an operator acting on the ROI boundary [40].

The functionals Φ_m^2 and Φ_b^2 must be minimised as well as Φ_c^2 and this

is referred to as the mechanical regularisation. However, such a minimisation is an ill-posed problem. A total functional, in which Φ_c^2, Φ_m^2 and Φ_b^2 are normalised and weighted, is considered. The three functionnals are then respectively normalised by $\{v\}^t[M]\{v\}$, $\{v\}^t[K]^t[K]\{v\}$ and $\{v\}^t[L]^t[L]\{v\}$. $\{v\}$ is a displacement field chosen to be in the form of a plane wave, $v(x) = v_0 e^{ik.x}$, where v_0 is the wave amplitude and k the wave vector. The total functional is then expressed as:

$$\Phi_t^2 = \left(\frac{1}{1 + w_m + w_b}\right)(\tilde{\Phi}_c^2 + w_m\tilde{\Phi}_m^2 + w_b\tilde{\Phi}_b^2), \tag{6}$$

where:

$\tilde{\Phi}_c^2$, $\tilde{\Phi}_m^2$ and $\tilde{\Phi}_b^2$ are normalised residuals.

w_m and w_b are weights defined by k and by the regularisation length scales l_m and l_b in pixels [40].

The minimisation of Φ_t^2 acts as a fourth-order low-pass filter on the displacement field [40]. It is worth noting there are now two representations of the displacement field. Indeed, the mechanical equations lead to nodal displacements whereas residuals lead to pixel displacements. The conversion from pixel to nodal displacements is performed by a linear interpolation.

The introduced correlation algorithm presents several benefits. First, in terms of displacement error, the global approach out-performs local approaches based on quadrilateral element subsets [40]. To reach equivalent uncertainty, local approaches use filtering processes that can result in inappropriate approximations. This is the case for instance when the tested material presents inhomogeneous properties. Second, local DIC uncertainty increases exponentially with the inverse of the subset size [49,50]. For the presented global approach, the uncertainty tends to saturate when the mesh size decreases. Consequently, it is possible to compute correlations using 1 pixel-sized elements while local approaches require subset sizes of 10 pixels and more [40]. Considering these assets of such algorithm, CorreliRT3 has been applied to the characterisation of ferroelectrics. The whole experimental setup and its reliability to measure ferroelectric strains are presented in the next parts.

3. Experimental setup

3.1. Measurement device

The experimental setup is described in Fig. 1. The setup is designed to apply an electric field E_3 up to 4 kV/mm to the sample, to measure the induced electric displacement D_3 and to measure the sample strain components S_{33} and S_{11} using DIC and S_{33} using a CCD laser displacement sensor. The sample is a 4 × 4 × 4 mm soft PZT (NCE55, Noliac) with silver electrodes. The piezoelectric and dielectric coefficients of this material are given in Table 1.

The high voltage, used to impose the electric field E_3, is produced by a Trek 20/20C HS high voltage amplifier. For insulation purpose, the sample is immersed in a PTFE container filled with insulating fluid (Fluorinert™ FC-770, 3 M). The electric displacement D_3 is measured from the upper electrode of the sample. The electrode is accessed using a rod (diameter 4 mm) sliding in a bracket, both conductive. The contact between the rod and the sample is ensured using a spring. Because of the small stiffness of the spring (1 N/mm), the stress induced by the rod is neglected. The conditioner used to obtain D_3 is an operational amplifier integrator circuit [51,52]. Integrating capacitors of 100 nF to 2000 nF are used to measure the sample response under electric fields from 10 V/mm to 4 kV/mm. The sample elongation ΔL_3 is measured using the CCD laser sensor LK-G10 connected to a LK-GD500 controller from Keyence. The sensor is placed above the rod (see Fig. 1a). The mean longitudinal strain of the sample is obtained from:

$$S_{33} = \frac{\Delta L_3}{L_3}, \tag{7}$$

with $L_3 = 4\,mm$.

The electric field E_3 is imposed using a real-time DSpace hardware module which has a maximum sampling frequency of 50 kHz. The elongation ΔL_3 and the electric displacement D_3 are recorded using the same module. These three variables are monitored on a first computer with MATLAB Simulink associated to a Graphic User Interface (DSpace ControlDesk, see Fig. 1b) .

During experiments, a lateral face of the sample is imaged with a

Table 1
Noliac NCE55 piezoelectric and dielectric coefficients from datasheet.

Parameter	d_{33} ($\times 10^{-12}\,m/V$)	d_{31} ($\times 10^{-12}\,m/V$)	ε_{33} / ε_0
Value	670	−260	5000

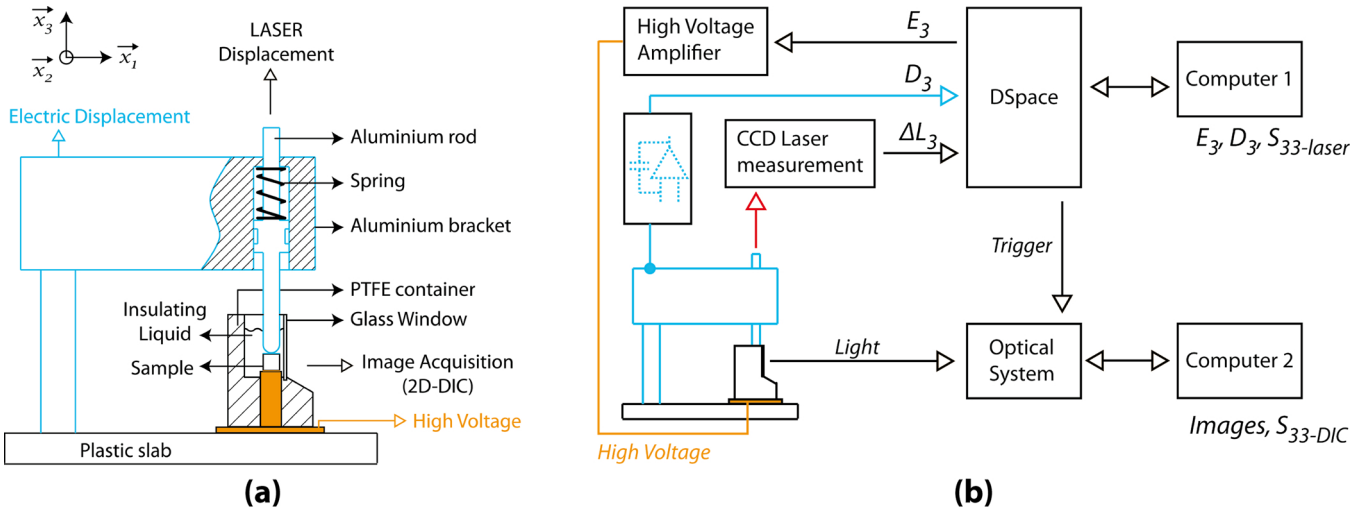

Fig. 1. Schematic drawing of the sample measurement device (a) and illustration of the whole experimental setup (b).

Ximea MD091MU-SY camera (14 bits monochrome, 3380 × 2708 px, 5 FPS maximum) mounted on a Questar QM100 MKIII. A visual access to the sample is ensured using a flat glass window (1 mm thick) mounted on a side of the PTFE container. The whole optical system is placed at 37.5 cm from the sample surface. In this condition, the aperture is f/7, the optical resolution is around 5 µm and the spatial sampling is 1.21 µm/px. The sample lighting is produced by a LLS 3 LED light source (SCHOTT North America, Inc.) and oriented with an optical fibre. The camera is triggered by the DSpace module to synchronise the image acquisition with the electric field. A second computer controls the camera using a MATLAB program. The program receives and stores the images using the TIFF format, without data compression. It also integrates a focusing and parallelism calibration function based on image gradient analysis. This function allows the mean image resolution to be maximised and ensures the angle between the sample surface and the camera sensor plane to be less than 0.2°. Once images are acquired, they are correlated in a post-processing step with the 2D-DIC MATLAB program Correli RT3 [40,42]. The displacement and strain fields (longitudinal and transverse) of the sample are then obtained. All DIC computations are made using the regularisation lengths $l_m = 2 \times l_b = 400\,px$. With these values, the computation time is about 1 min per image, which is far faster than previous PZT studies using DIC [38,39].

3.2. Speckle pattern

Samples studied using DIC must contain a tracking texture to evaluate displacements. The natural texture of the sample can be used for this purpose or an artificial texture can be applied to it to optimise the correlation quality. Generally, the texture is created by applying black/white dots randomly or periodically positioned on a white/black background. The image of such texture is commonly referred to as a "speckle pattern". Random speckles are usually preferred to periodic speckles since it creates unique local textures. This property allows subsets (or elements) to be differentiated from their neighbours and allows correlation conflicts to be avoided. In this paper, a random speckle pattern is used as tracking texture.

Several studies were carried out in the past to identify the influence of the speckle characteristics (for instance, contrast, density or speckle size) on the correlation quality [46,53–55]. One way to quantify the texture quality is to compute the image gradient $\nabla f(x)$. Indeed, in Eq. (1) the displacement $u(x)$ is weighted by $\nabla f(x)$. Thus, the displacement resolution is proportional to the inverse of $\nabla f(x)$ [56]. As the speckle pattern corresponds to the grey level variation function $f(x)$, $\nabla f(x)$ directly reflects the speckle quality. This quality is maximised when the Mean Intensity Gradient (MIG) of the entire image is maximized [54,55].

Using the MIG and simulated images, we have recently identified the optimal density and speckle radius of specific speckle patterns [57]. Speckles made of circular black dots randomly positioned onto a white background were considered. The simulations also accounted for the optical resolution and the spatial sampling of the experimental setup. It was shown that the MIG is maximised for a speckle density of 0.5 and for diameters ranging from 6 to 17 µm, depending on the optical magnification used [57]. Considering these results, the speckle is experimentally produced by depositing black circular particles (toner powder with ~10 µm diameter per grain) onto a white acrylic layer. Both white paint and powder are deposited on the specimens using the airbrush Badger Sotar 20/20. An example of the speckle obtained with this method is shown in Fig. 2.

4. Characterisation of the DIC technique

The sample is subjected to a 4 kV/mm triangular electric field at 10 mHz. During this test, the sample is imaged to compute strains *a posteriori* by DIC using 64 px sized T3 elements. For comparison purpose, the strain is also recorded with the CCD laser sensor. The triangle waveform is used instead of a sine because the number of images is limited to 350 by the computer memory. The triangle then helps to distribute images around the coercive field. The image acquisition frequency is set to 3.5 Hz (350 images per hysteresis loop) with an exposure time of 4 ms per image (i.e. 0.004% of the electric field period). The polarisation of the sample is measured using a fixed capacitance of 2.057 µF.

In this part, the displacement and strain fields obtained by DIC at $E_3 = -2$ kV/mm are first shown and discussed. Then, the mean value of the DIC strain fields are collected to plot the sample *S-E* loop. The *S-E* loop is discussed and compared to the *S-E* loop obtained with the CCD laser sensor.

4.1. Displacement and strain field measurements

Fig. 3 shows the DIC displacement and strain fields at $E_3 = -2$ kV/mm.

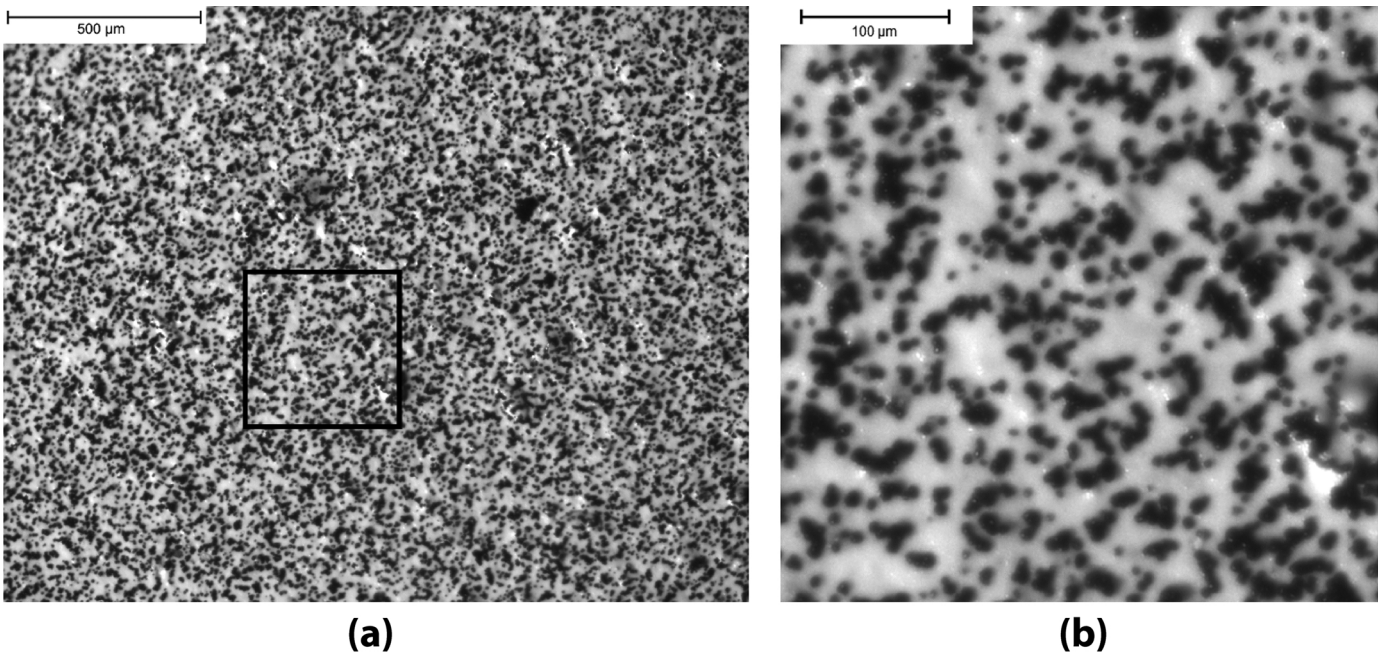

Fig. 2. Pictures at two different magnifications (a) and (b) of a speckle made on a piezoelectric material with white paint and toner powder.

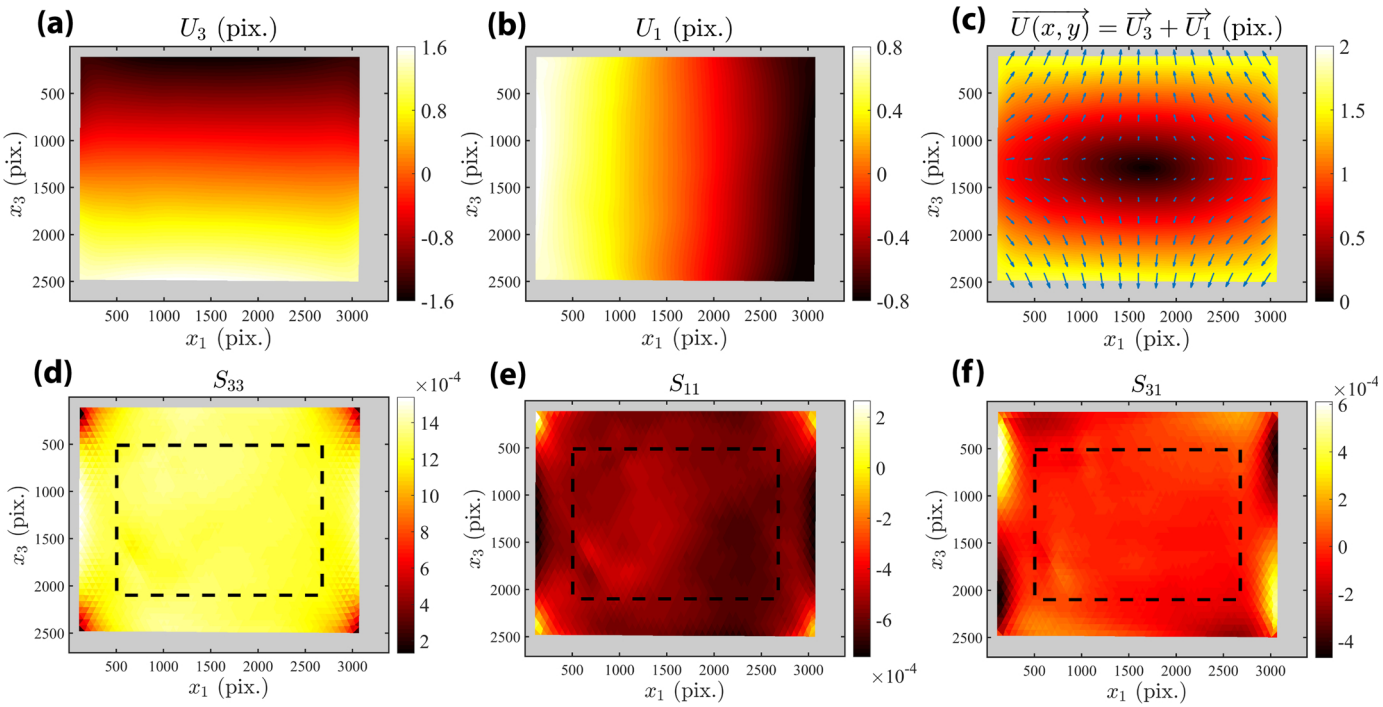

Fig. 3. Longitudinal (a) and transverse displacement fields (b) measured using DIC on a NCE55 sample under −2 kV/mm. Vector displacement field is plotted on graph (c). Longitudinal (d), transverse (e) and shear (f) strain fields are obtained from displacement fields using 64 px sized T3 elements. The black dashed rectangles represent the zone used for computing mean and standard deviation values.

Fig. 3a and Fig. 3b gives the longitudinal and the transverse displacement field, respectively. The displacement reference point is approximatively the image centre (see Fig. 3c) because rigid body motions were removed. The displacements are expressed in pixels since they were computed from numerical images. In real space, the overall longitudinal displacement is ~3.87 µm and the overall transverse displacement is ~1.94 µm since the spatial sampling period is 1.21 µm/px. As expected, the displacement field exhibits a longitudinal elongation and a transverse contraction by comparison to the reference state ($E_3 = 0$).

Fig. 3d, e and f present the DIC longitudinal, transverse and shear strain field at $E_3 = -2$ kV/mm, respectively. The strains are computed from Fig. 3a and b in a finite element sense. Using the nodal displacements of the T3-meshing, the Constant Strain Triangle (CST) method [58] is applied to obtain the strain on each element. The longitudinal strain (Fig. 3d) fluctuates between 0.2×10^{-3} and 1.5×10^{-3}. The highest fluctuations are localised at the edges of the strain field. The same observations are made on the transverse and shear strains (Fig. 3e and f). These fluctuations are believed to be correlation errors since the field is discontinuous in the corresponding regions. The boundary regularisation of the DIC algorithm may not be sufficient to compensate for the displacement discontinuity. However, it cannot be exclude that these fluctuations are due to an inhomogeneous electric field at the sample boundary.

To discard the strain fluctuations at the edges, each strain field is studied in its central part. This part is indicated in the figures by a dashed rectangle and contains 1700 elements. The mean and standard deviation of the strain are computed in this zone. Values are reported in Table 2. The observed magnitude, about 10^{-3}, are expected for this class of materials. Standard deviations are less than $\sim 5 \times 10^{-5}$ for all strain fields (approximatively 5% of the strain amplitudes, which is $\sim 10^{-3}$) meaning that the strain fields are satisfactorily homogeneous in the studied area. Regarding the shear strain, the mean value is 2.35×10^{-5} with a standard deviation of 3.28×10^{-5}. The mean value is attributed to a measurement error and is neglected since it is 23 times lower than the transverse strain .

Table 2
Mean and standard deviations of the strain fields at E = −2 kV/mm (Fig. 3).

	Measurement: Mean Value	Measurement: Standard Deviation
S_{33} (longitudinal)	1.29×10^{-3}	4.01×10^{-5}
S_{11} (transverse)	-0.550×10^{-3}	5.15×10^{-5}
S_{31} (shear)	-0.0235×10^{-3}	3.28×10^{-5}

4.2. Ferroelectric measurement

Fig. 4 shows the macroscopic strain and polarisation as a function of the applied electric field. All measurements are made simultaneously. The polarisation (Fig. 4a) at saturation is 0.40 C/m² and the remanent polarisation is 0.34 C/m² which is consistent with other PZT studies [24,59]. The *P-E* loop exhibits a 5 V/mm difference between the negative and positive coercive field. This difference is not significant since it represents less than 1% of the coercive field.

The longitudinal strain (Fig. 4b) amplitude measured with DIC (blue curve) is of 3.80×10^{-3}. The electric field at the minimum strain is measured as 595 V/mm. This is in satisfying agreement with the CCD laser measurement. The strain hysteresis is however larger for the CCD laser measurement than for the DIC measurement. This is presumable the result of the sliding friction between the rod and the bracket. Regarding the noise on the red curve, it is caused by environmental vibrations transmitted from the floor to the setup. This noise is not visible on DIC measurements since DIC is, in the present case, slightly sensitive to vibrations. Indeed, the effect of vibrations during an image acquisition corresponds to a sliding average filter. The light intensity is averaged in the motion direction during the exposure time. In the present case, the maximum vibration velocity is around 0.04 px/ms and the exposure time is set to 4 ms. Each image is then averaged over a maximum of 0.16 px. The spectral response of this filter has been numerically computed. Its spatial cut-off period has been found to be 0.27 px. This is 74 times less than the spatial cut-off period of the optical system, which is 20 px. The effect of vibrations are then neglected.

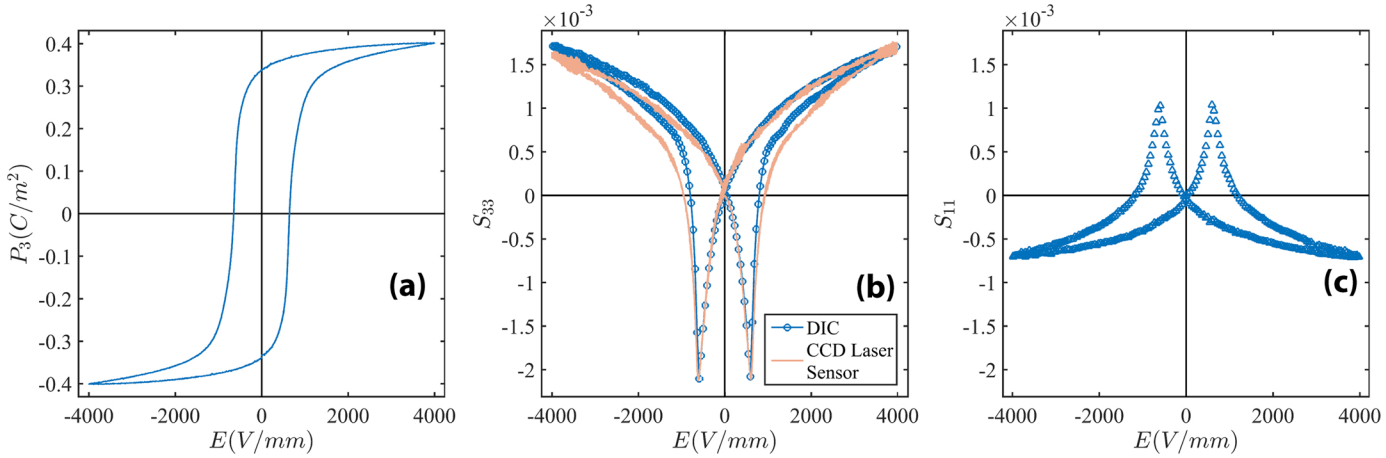

Fig. 4. Ferroelectric characterisation result for a triangle electric field (4 kV/mm at 10 mHz). Polarisation $\boldsymbol{P}_3$ (a), longitudinal strain $\boldsymbol{S}_{33}$ obtained by DIC (blue) and CCD laser sensor (orange) (b) and transverse strain $\boldsymbol{S}_{11}$ obtained by DIC (c) (For interpretation of the references to colour in this figure legend, the reader is referred to the web version of this article).

The transverse strain (Fig. 4c) amplitude is of 1.74×10^{-3}, which represents 46% of the longitudinal strain amplitude. Since the ratio is not equal to 50%, the process is not isochoric. Another important observation is the difference between the maximum strains at positive and negative electric fields (ΔS^+ and ΔS^-). The asymmetry factor $\gamma S = (\Delta S^+ - \Delta S^-)/(\Delta S^+ + \Delta S^-)$ is of 0.5×10^{-2} for the DIC measurement and of 1.2×10^{-2} for the laser measurement (Fig. 4b). The asymmetry of the transverse strain is smaller with a factor of 0.1×10^{-2}. These asymmetries are attributed to a measurement error and, regarding the DIC measurement, the asymmetry factors are acceptable.

It is possible to qualify further the DIC measurement by analysing the strain field distribution during the electric excitation. Fig. 5 shows the standard deviations of the DIC strain fields (dashed rectangle of Fig. 3d, e and f) as a function of the electric field. The values remain below 1.2×10^{-4} for a decreasing electric field. This represents less than 5% of the maximum transverse strain. The strain fields can then be considered as homogeneous. However, this is not true for increasing electric fields, two peaks in standard deviation are observed. These peaks do not reflect

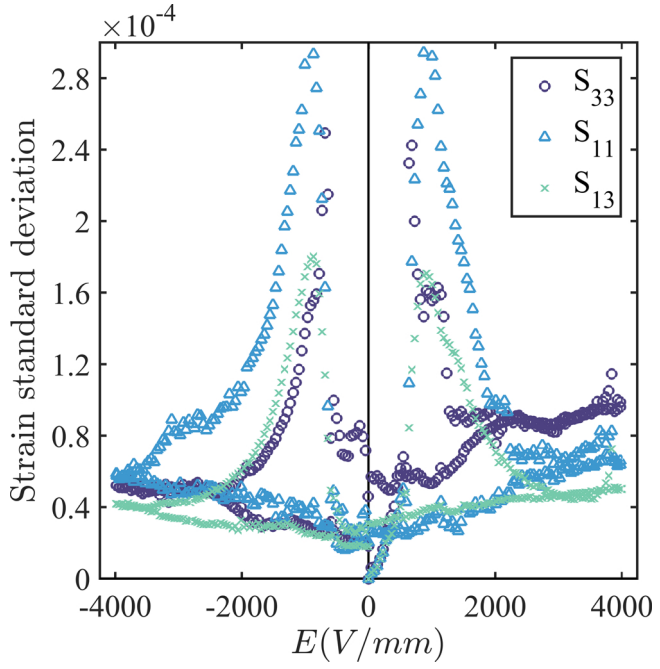

Fig. 5. – Standard deviation of strain fields $\boldsymbol{S}_{33}$, $\boldsymbol{S}_{11}$ and $\boldsymbol{S}_{13}$ as a function of the electric field.

an experimental error and are related to the sample. Indeed, the peaks are reproducible and the fluctuations observed in the strain fields were found to be systematic, not random. An explanation for these fluctuations is the polarisation reversal since the peaks position matches the coercive field. Around the coercive field, the polarisation of local dipoles is reversed and this reversal does not occur continuously due to dissipation effects. Thus, heterogeneities are expected in the strain field. The order of magnitude of the heterogeneities is relatively high with a standard deviation of 3×10^{-4} for the transverse strain. The electric field frequency might be too high to prevent dynamic effects to appear at the coercive field.

In this part, it was shown that Digital Image Correlation algorithms based on global approaches are efficient tools to characterise ferroelectric strains. Considering elements with 64 px size, the total strain measurement error for each element does not exceed 1.2×10^{-4} under quasi-static measurement condition. With such elements, the mean value of the strain is calculated over 1700 elements. Assuming that the error randomly follows a normal distribution, this leads to a $1.2 \times 10^{-4}/\sqrt{1700} = 3 \times 10^{-6}$ error on the mean value of the strain. Consequently, it is theoretically possible to characterise not only ferroelectric strains but also piezoelectric strains using the presented setup. In order to verify this observation, the sample behaviour is characterised in the next part from sub-coercive to high electric fields.

5. Piezoelectric to ferroelectric characterisation

In this part, the sample is characterised from small (piezoelectric behaviour) to high electric fields (ferroelectric behaviour) with the same setup (see Section 3). For this purpose, two experiments are proposed. For both experiments, the sample is first depoled and repoled once at 4 kV/mm during 1 min. The depolarisation process is made according to the anhysteretic bias field method [61] (bias field of 0 V/mm, frequency of 0.5 Hz, duration of 60 s and exponential damping factor of 0.015). The first experiment consists in subjecting the sample to 50 mHz bipolar sinusoidal electric field with increasing amplitudes. The polarisation and the DIC longitudinal and transverse strains are acquired. The second experiment is identical, but performed under unipolar sinusoidal electric field. The sine waveform is chosen so as to compare the results (see Section 6) to other PZT studies. The image acquisition frequency is 5 Hz (100 points per cycle). All strains were obtained by computing the mean value of the DIC strain field centre.

5.1. Bipolar electric field

Fig. 6 presents $P(E)$ and $S(E)$ loops for bipolar loadings. On both polarisation and strain, the sample exhibits an overall linear behaviour and

small hysteresis until 200–250 V/mm. Then, an inflection point appears at the bottom part of the cycles. As the material is polarised, saturation is reached for positive electric fields but not for negative ones, which creates the inflexion. At 550 V/mm, the negative coercive field is reached and the hysteresis becomes substantial. The polarisation even reaches -0.3 C/m^2 at 600 V/mm which approximatively corresponds to half the major cycle amplitude: the material is depolarised and repolarised during this cycle. On the strain loop, a new wing appears and the loop becomes an asymmetric butterfly loop. Above 600 V/mm, the cycle amplitude grows and the asymmetry factor of the butterfly loop decreases. At 4000 V/mm, the cycles are symmetric: the preferred orientation of domains (known as internal or imprint electric field [60,62,63]) due to the initial pre-polarisation has vanished. The loops are then major loops. More details are given and analysed from these graphs in the discussion part.

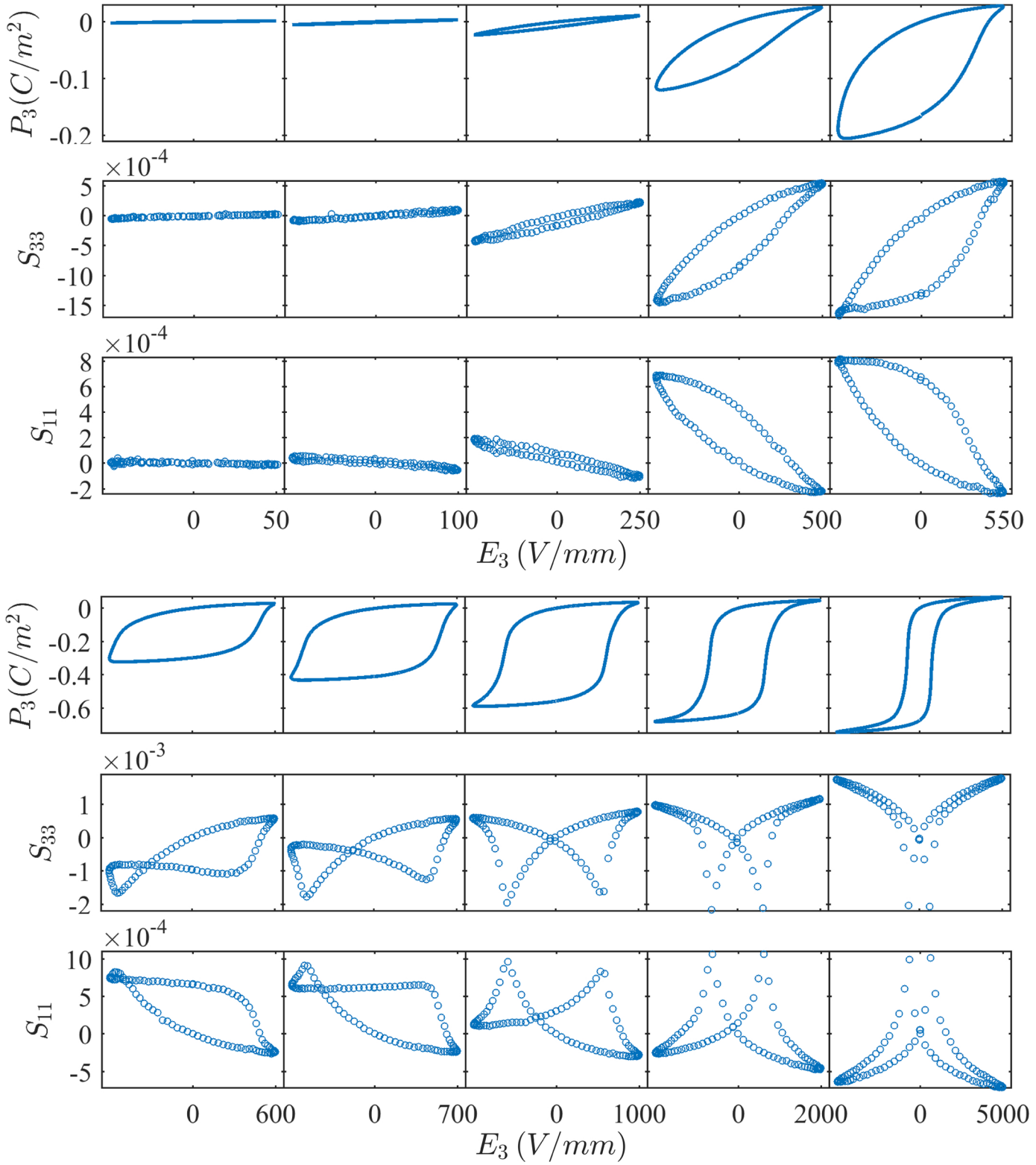

Fig. 6. Polarisation $\boldsymbol{P}_3$, longitudinal strain $\boldsymbol{S}_{33}$ and transverse strain $\boldsymbol{S}_{11}$ under growing bipolar sinusoidal electric field (50 mHz). Before measurements, the sample (NCE55) was initially poled at 4000 V/mm during 1 min.

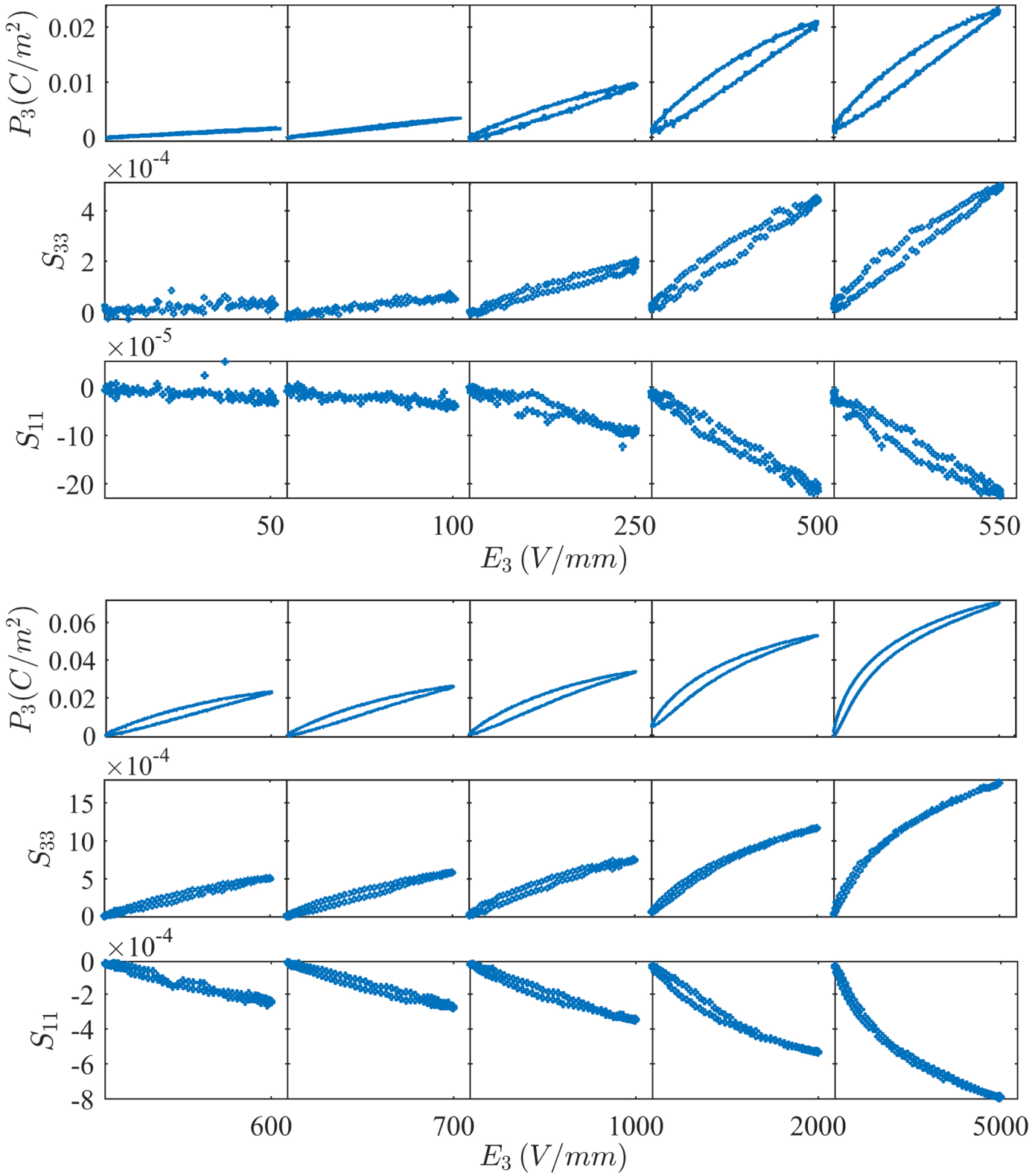

Fig. 7. Polarisation P_3, longitudinal strain S_{33} and transverse strain S_{11} under growing unipolar sinusoidal electric field (50 mHz). Before measurements, the sample (NCE55) was initially poled at 4000 V/mm during 1 min.

5.2. Unipolar electric field

The $P(E)$ and $S(E)$ loops for unipolar loadings are shown in Fig. 7. The material is electrically loaded along the direction of pre-polarisation. The polarisation is thus never reversed; this experiment shows the behaviour of the material close to the saturation state. As a consequence, all cycles are narrow compared to bipolar cycles (small dissipation). The cycles are elliptic until 250 V/mm and begin to curve downward from 500 V/mm. Consequently, the polarisation and strains increase more at low fields than at high fields. This was expected since the material is electrically saturated at high fields, hence, the extrinsic effect cannot contribute anymore to the rise of polarisation and strain. A detailed analysis of the susceptibility and piezoelectric coefficients as a function of the electric field is presented in the next part.

6. Discussion

The bipolar and unipolar characterisations shown in Figs. 6 and 7 respectively are analysed by extracting the apparent piezoelectric coefficients and susceptibility:

$$d_{33}^{*} = \frac{\Delta S_{33}}{\Delta E_3},\ d_{31}^{*} = \frac{\Delta S_{11}}{\Delta E_3} and\ \chi_{33}^{*} = \frac{\Delta P_3}{\Delta E_3} \quad (8)$$

where ΔE_3 is the electric field variation, ΔS_{33} the longitudinal strain variation, ΔS_{11} the transverse strain variation and ΔP_3 the polarisation variation. These parameters are computed with an ordinary least square regression over all points of each cycle of Figs. 6 and 7 (*S(E)* for d_{33}^{*} and d_{31}^{*} and *P(E)* for χ_{33}^{*}). They are called "apparent" since they differ from the actual intrinsic coefficients. The dissipated energy is also obtained from Figs. 6 and 7. It is computed as the parametric integral of a *P(E)* cycle and represents the volume density of electrical energy dissipated per cycle. Results are presented in Fig. 8 (bipolar electric field) and Fig. 9 (unipolar electric field). All parameters are plotted as function of the maximum electric field. The coefficients d_{33}^{*}, d_{31}^{*} and χ_{33}^{*} are computed for cycles ranging from 75 to 550 V/mm. Under 75 V/mm, the measurement noise is too high to obtain reliable results. Above 550 V/mm, the coercive field is exceeded.

For bipolar electric fields, the piezoelectric coefficients d_{33}^{*} and d_{31}^{*} evolve linearly with the maximum electric field (Fig. 8a and b). This

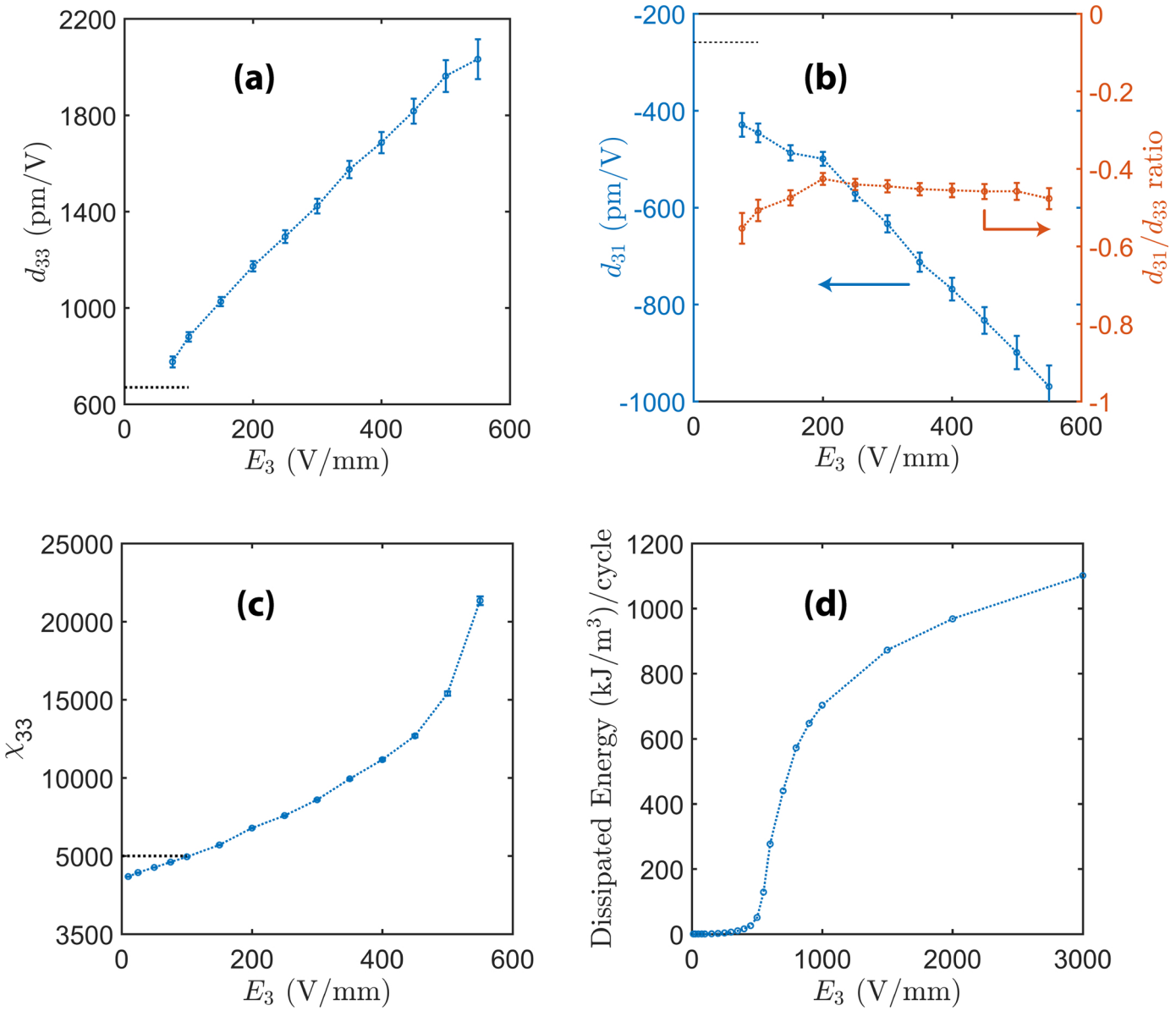

Fig. 8. Apparent d_{33}^{*} (a), d_{31}^{*} (b), susceptibility χ_{33}^{*} (c) and dissipated energy (d) measured on cycles of Fig. 6 (bipolar growing E) and plotted as function of the maximum electric field. The dotted lines (Fig. 8a–c) indicate the manufacturer values.

trend is in agreement with previous studies on soft PZT [17,24,64,65]. The values of the coefficients at low electric fields are consistent with the manufacturer data (d^*_{33} of 670 pm/V and a d^*_{31} of 260 pm/V, see Table 1). However, these values increase significantly with the electric field. At 550 V/mm, these values are multiplied by 3 for d^*_{33} and by 4 for d^*_{31}. The approximation of piezoelectric behaviour (linear behaviour) is then restricted to electric fields under 75 V/mm for this material. Regarding the d^*_{31}/d^*_{33} ratio, the linear evolution of the coefficients (Fig. 8a and b) makes it quasi-constant. Above 200 V/mm, values are bounded between −0.43 and −0.48.

The evolution of the susceptibility χ^*_{33} (Fig. 8c) does not follow the evolution of the piezoelectric coefficients. The susceptibility increases linearly only at low electric fields. This observation is typical for PZT and has already been reported [17,24,51,64–66]. The non-linear increase around the coercive field is due to the squared-shape polarisation loop. As soon as the electric field gets close to the coercive field, the polarisation amplitude increases rapidly. However, this increase is associated to a high dissipation increase (100 kJ/m^3/cycle between 450 and 550 V/mm, Fig. 8d). The value of χ^*_{33} then corresponds only to the global sensitivity $\frac{\Delta P}{\Delta E}$ of the cycle.

The coercive field shows a clear frontier between apparent piezoelectricity and ferroelectricity. On the dissipated energy (Fig. 8d), the values are less than 0.22 kJ/m^3/cycle for electric fields lower than 100 V/mm. In this electric field range, the material behaviour (Fig. 6) is linear and reversible. From 100 V/mm to the near coercive field (500 V/mm), the dissipation increases to 51 kJ/m^3/ cycle and is no more negligible. This part is known as the Rayleigh region [17,66,67]. Above 500 V/mm, the dissipation rises rapidly and reaches 1100 kJ/m^3 at 3000 V/mm: the domain switching processes responsible of ferroelectricity become here prominent [17].

For unipolar electric fields (Fig. 9), results for $E_3 < 100$ V/mm are comparable to results for bipolar electric fields (see Table 3). This was

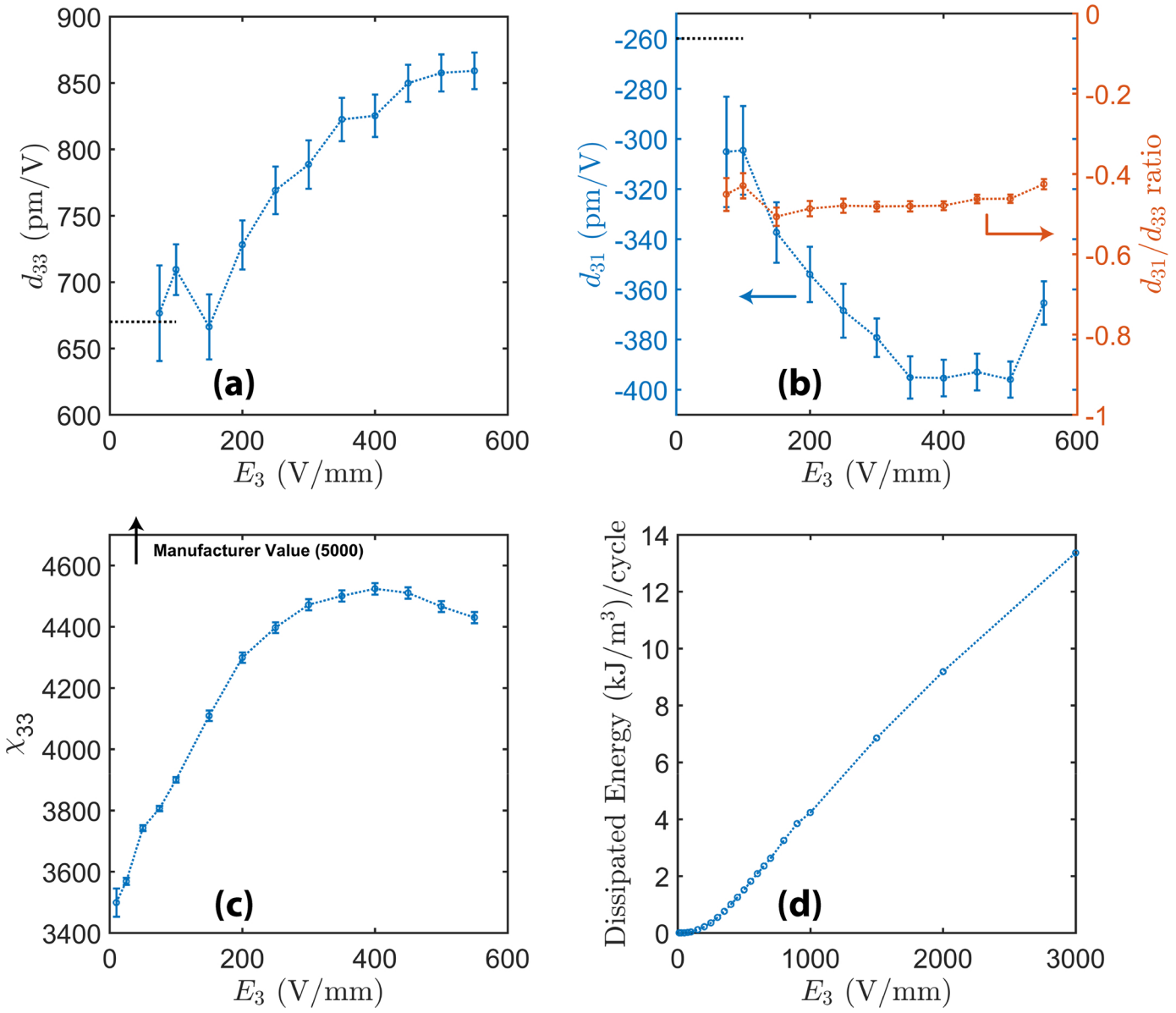

Fig. 9. Apparent d^*_{33} (a), d^*_{31} (b), susceptibility χ^*_{33} (c) and dissipated energy (d) measured on cycles of Fig. 7 (unipolar growing E) and plotted as function of the maximum electric field. The dotted lines (Fig. 9a–c) indicate the manufacturer values.

Table 3
Apparent piezoelectric and dielectric coefficients obtained at 75 and 500 V/mm. Values obtained at 75 V/mm are compared with the manufacturer data.

	At 75 V/mm			At 500 V/mm		
	$d_{33}^*(\times 10^{-12}$m/V)	$d_{31}^*(\times 10^{-12}$m/V)	χ_{33}^*	$d_{33}^*(\times 10^{-12}$m/V)	$d_{31}^*(\times 10^{-12}$m/V)	χ_{33}^*
Bipolar field	776	−429	4606	1963	−899	15400
Unipolar field	677	−305	3806	858	−396	4466
Manufacturer data	670	−260	5000	–	–	–

expected since the initial polarisation state of the material is the same in both cases. However, a difference appears when the electric field is increased. The piezoelectric coefficients for unipolar electric fields remain small compared to bipolar electric fields (d_{33}^* of 860 pm/V and d_{31}^* of −400 pm/V at 500 V/mm). Moreover, the values increase non-linearly (saturation at 500 V/mm). The d_{31}^*/d_{33}^* ratio is comparable to the ratio obtained for bipolar fields above 200 V/mm.

The evolution of χ_{33}^* is similar to the evolution of the piezoelectric coefficients. The susceptibility moves up linearly (from 3800 to 4500) and then saturates (around 400 V/mm). Above 400 V/mm, values decrease due to the apparition of the downward curvature in the $P(E)$ cycles (see Fig. 7). For these electric fields, as for bipolar electric fields, the computed χ_{33}^* does not refer to susceptibility anymore. Regarding the dissipated energy (Fig. 9d), values are extremely low (82 times less than bipolar field dissipations). This was expected since the material is used far from its coercive field (−600 V/mm).

7. Conclusion

The Digital Image Correlation measurement method was used to characterise PZT strains (longitudinal and transverse) from low to high electric fields. The speckle pattern, the global DIC algorithm and the mechanical regularisation process allowed strains to be measured with satisfying resolution (standard deviation of $\sim 3 \times 10^{-6}$ on the mean strain) and satisfying computing time (~1 min per image). It is worth noting that the regularisation takes into account the mechanical admissibility of the displacement field. This work has improved the DIC technique for the characterization of piezoelectric and ferroelectric strains. Moreover, the DIC setup showed interesting advantages such as non-sensitivity to micrometre scaled vibrations and the ability to identify test heterogeneities.

The DIC setup has also proved its ability to measure soft PZT properties from 50 to 5000 V/mm (bipolar and unipolar). It is believed that smaller electric fields could be studied by conducting the measurements in the air, which would remove the errors induced by the electrical insulation liquid. Considering that DIC is contactless, the technique appears to be a good alternative for the measurement of low electric field behaviour. Indeed, contrary to LVDT or strain gages, DIC provides results where the measurement has not interacted with the test conditions. The limit of the presented application is that the measured parameters are obtained from a sample lateral face, where boundary effects can lead to inhomogeneous properties. However the heterogeneities are mainly concentrated at the sample corners. In the present case, the centre part of the images provides reliable results.

The benefits of 2D-DIC for the study of ferroelectric materials are numerous. The measurement scale is not physically limited like for other methods. For instance, the microscopic and nanoscopic scales could be investigated by DIC using not optical, but SEM (Scanning Electron Microscope) images. It could then be possible to characterise the behaviour at the microstructure level. For example, the strain at domain or grain boundaries could be investigated. Finally, DIC is used here for quasi-static and high-resolution measurement but has a high-frequency potential with high speed cameras (up to 100 kHz and more with reduced digital resolution).

Acknowledgments

This work was supported by the Automotive Mechatronics Chair, a co-operation between Faurecia, CentraleSupélec and Esigelec.

References

[1] R. Booth, P. Goldsmith, Detecting finger gestures with a wrist worn piezoelectric sensor array, 2017 IEEE International Conference on Systems, Man, and Cybernetics (SMC) (2017) 3665–3670.
[2] I. Mahbub, S.A. Pullano, H. Wang, S.K. Islam, A.S. Fiorillo, G. To, A low-power wireless piezoelectric sensor-based respiration monitoring system realized in CMOS process, IEEE Sens. J. 17 (no. 6) (2017) 1858–1863.
[3] J. Carioli, A. Delnavaz, R.J. Zednik, J. Voix, Piezoelectric earcanal bending sensor, IEEE Sens. J. 18 (no. 5) (2018) 2060–2067.
[4] H. Borgmann Bremen, Germany: MESSE BREMEN, WFB Wirtschaftsförderung Bremen GmbH, Bremen, Germany15th International Conference on New Actuators & 9th International Exhibition on Smart Actuators and Drive Systems2016, in: H. Borgmann (Ed.), 15th International Conference on New Actuators & 9th International Exhibition on Smart Actuators and Drive Systems (2016).
[5] C. Dagdeviren, B. Yang, Y. Su, P. Tran, P. Joe, E. Andersion, J. Xia, V. Doraiswamy, B. Dehdashti, W. Feng, B. Lu, R. Poston, Z. Khalpey, R. Ghaffari, Y. Huang, M. Slepian, J. Rogers, Conformal piezoelectric energy harvesting and storage from motions of the heart, lung, and diaphragm, PNAS 111 (5) (2013) 1927–1932.
[6] K.F. Kwok, P. Dong, K.W.E. Cheng, K.W. Kwok, Y.L. Ho, X.X. Wang, H. Chan, General study on piezoelectric transformer, First International Conference on Power Electronics Systems and Applications (2004) IEEE.
[7] R. Cuppens, P.K. Larsen, G.A.C.M. Spierings, Ferroelectrics for non-volatile memory, Microelectron. Eng. 19 (1992) 245–252.
[8] N.M. D'souza, V. Mathew, Tunable filter using ferroelectric-dielectric periodic multilayer, Appl. Opt. 54 (no. 9) (2015) 2187–2192.
[9] Z. Wang, S. Khandelwal, A.I. Khan, Ferroelectric oscillators and their coupled networks, Ieee Electron Device Lett. 38 (no. 11) (2017) 1614–1617.
[10] E. Sawaguchi, Ferroelectricity versus antiferroelectricity in the solid solutions of $PbZrO_3$ and $PbTiO_3$, J. Phys. Soc. Jpn. 8 (no. 5) (1953) 615.
[11] P.W. Forsbergh Jr, Encyclopedia of Physics / Handbuch der Physik book series (HDBPHYS, volume 4 / 17), Dielectrics 4/17 (1956) 264–392 ch. Piezoelectricity, Electrostriction and Ferroelectricity.
[12] R. Herbiet, U. Robels, H. Dederichs, G. Arlt, Domain wall and volume contributions to material properties of PZT ceramics, Ferroelectrics 98 (1989) 107–121.
[13] D. Damjanovic, D.V. Taylor, Contributions to the nonlinear dielectric and piezoelectric response of ferroelectric thin films and ceramics, Ferroelectrics 221 (1999) 137–146.
[14] L. Daniel, D. Hall, P.J. Withers, A multiscale model for reversible ferroelectric behaviour of polycrystalline ceramics, Mech. Mater. 71 (2014) 85–100.
[15] K.G. Webber, E. Aulbach, J. Roedel, High temperature blocking force measurements of soft lead zirconate titanate, J. Phys. D-Appl. Phys. 43 (36) (2010) 365401.
[16] M. Davis, Phase transitions, anisotropy and domain engineering: The piezoelectric properties of relaxor-ferroelectric single crystals, Doctoral dissertation, Ecole Polytechnique Fédérale de Lausanne, Lausanne, Swiss) (2006).
[17] D. Hall, Nonlinearity in piezoelectric ceramics, J. Mater. Sci. 36 (2001) 4575–4601.
[18] F.H. Schader, G. Rossetti Jr, J. Luo, K.G. Webber, Piezoelectric and ferroelectric properties of $< 001 >_C$ $Pb(In_{1/2}Nb_{1/2})$ O_3-$Pb(Mg_{1/3}Nb_{2/3})O_3$-$PbTiO_3$ single crystals under combined thermal and mechanical loading, Acta Mater. 126 (2017) 174–181.
[19] R. Hühne, S. Trommler, P. Pahlke, L. Schultz, Low temperature performance of $Pb(Mg_{1/3}Nb_{2/3})_{0.72}Ti_{0.28}O_3$ single crystals mapped by metallic and superconducting thin films, 2014 Joint IEEE International Symposium on the Applications of Ferroelectric, International Workshop on Acoustic Transduction Materials and Devices & Workshop on Piezoresponse Force Microscopy, (2014).
[20] K.G. Webber, E. Aulbach, T. Key, M. Marsilius, T. Granzow, J. Rödel, Temperature-dependent ferroelastic switching of soft lead zirconate titanate, Acta Mater. 57 (2009) 4614–4623.
[21] J. Shieh, Y. Shu, J. Yeh, J. Yen, Large strain actuation in barium titanate single crystals under stress and electric field," in 5th Australasian Congress on Applied Mechanics, ACAM 2007 (2007).
[22] D. Taylor, D. Damjanovic, N. Setter, Nonlinear contributions to dielectric and piezoelectric properties in PZT thin films, Ferroelectrics 224 (1999) 299–306.
[23] R. Dittmer, K.G. Webber, E. Aulbach, J. Wook, X. Tan, J. Rödel, Optimal working

regime of lead-zirconate-titanate for actuation applications, Sens. Actuators A Phys. 189 (2013) 187–194.
[24] D. Damjanovic, The Science of Hysteresis 3 Elsevier, 2006, pp. 337–452 ch. Hysteresis in piezoelectric and ferroelectric materials.
[25] B. Pan, D. Wu, Z. Wang, T. Xia, High-temperature digital image correlation method for full-field deformation measurement at 1200°C, Meas. Sci. Technol. 22 (2011) 015701.
[26] M. Mahal, T. Blanksvärd, T. Tä, G. Sas, Using digital image correlation to evaluate fatigue behavior of strengthened reinforced concrete beams, Eng. Struct. 105 (2015) 277–288.
[27] P. Lall, K. Mirza, J. Suhling, A study on the effect of aging on thermal cycling reliability of Sn-Ag-Cu interconnects using digital image correlation, 15th IEEE Intersociety Conference on Thermal and Thermomechanical Phenomena in Electronic Systems (ITherm), (2016).
[28] M.W. Nansteel, C.C.-T. Chen, Digital image correlation: a measurement tool for the study of explosive effects, Technologies for Homeland Sec, (2009).
[29] J.-F. Witz, P. Lecomte-Grosbras, A. Morch, C. Martel, F. Lesaffre, M. Brieu, Digital image correlation for large strain, in: M. Sutton, P. Reu (Eds.), International Digital Imaging Correlation Society, 2016.
[30] F. Zighem, M. Belmeguenai, D. Faurie, H. Haddadi, J. Moulin, Combining ferromagnetic resonator and digital image correlation to study the strain induced resonance tunability in magnetoelectric heterostructures, Rev. Sci. Instrum. 103905 (2014) 85.
[31] R.F. Elhajjar, C.T. Law, Magnetomechanical local-global effects in magnetostrictive composite materials, Model. Simul. Mat. Sci. Eng. 23 (2015) 075002.
[32] F.M. Sánchez-Arévaloa, T. García-Fernández, G. Pulos, M. Villagrán-Muniz, Use of digital speckle pattern correlation for strain measurements in a CuAlBe shape memory alloy, Mater. Charact. 60 (2009) 775–782.
[33] O.E. Ozbulut, S. Daghash, M.M. Sherif, Shape memory alloy cables for structural applications, J. Mater. Civil Eng. (ASCE) 2015 (2015) 04015176.
[34] T.B.B.J. Meuris, Imaging methods for novel materials and challenging applications, chapter 40 - thermal analysis of PZT thin films using digital image correlation, ser, Conference Proceedings of the Society for Experimental Mechanics Series 3 (2012) 287–294.
[35] R. Bai, L. Wang, Z. Lei, H. Chen, Experimental and numerical analysis of interfacial fracture in piezoelectric composites, Optoelectron. Adv. Mater. 5 (no. 12) (2011) 1328–1335.
[36] M.H. Malakooti, H.A. Sodano, Noncontact and simultaneous measurement of the d33 and d31 piezoelectric strain coefficients, Appl. Phys. Lett. 102 (2013) p. 061901.
[37] M.H. Malakooti, H.A. Sodano, Direct measurement of piezoelectric shear coefficient, J. Appl. Phys. 113 (2013) 214106.
[38] D. Chen, M. Kamlah, Deformation in lead zirconate titanate ceramics under large signal electric field loading measured by digital image correlation, Rev. Sci. Instrum. 86 (2015) 113707.
[39] D. Chen, E. Carter, M. Kamlah, Deformation behavior of lead zirconate titanate ceramics under uniaxial compression measured by the digital image correlation method, Smart Mater. Struct. 25 (8pp) (2016) 097001.
[40] Z. Tomicevc, F. Hild, S. Roux, Mechanics-aided digital image correlation, J. Strain Anal. Eng. Des. 48 (5) (2013) 330–343.
[41] M.A. Sutton, W.J. Walters, W.H. Peters, W.F. Ranson, S.R. McNeil, Determination of displacements using an improved digital correlation method, Image Vis. Comput. 1 (no. 3) (1983) 133–139.
[42] F. Hild, S. Roux, Comparison of local and global approaches to digital image correlation, Exp. Mech. 52 (2012) 1503–1519.
[43] T.C. Chu, W.F. Ranson, M.A. Sutton, W.H. Peters, Applications of digital-image-correlation techniques to experimental mechanics, Exp. Mech. 25 (1985) 232–244.
[44] H.W. Schreier, J.R. Braasch, M.A. Sutton, Systematic errors in digital image correlation caused by intensity interpolation, Opt. Eng. 39 (no. 11) (2000) 2915–2921.
[45] L. Xiong, X. Liu, G. Liu, J. Liu, X. Yang, Q. Tan, Evaluation of sub-pixel displacement measurement algorithms in digital image correlation, International Conference on Mechatronic Science, (2011).
[46] M.A. Sutton, J.-J. Orteu, H.W. Schreier, Image Correlation for Shape, Motion and Deformation Measurements, Springer, 2009 iSBN : 978-0-387-78746-6.
[47] B.K.P. Horn, B.G. Schunck, Determining optical flow, Artif. Intell. 17 (1-3) (1981) 185–203.
[48] M.J. Black, Robust Incremental Optical Flow, Ph.D. dissertation, Yale University (1992).
[49] G. Besnard, F. Hild, S. Roux, "Finite-Element" displacement fields analysis from digital images: Application to Portevin - Le Châtelier bands, Exp. Mech. 46 (no. 6) (2006) 789–803.
[50] B. Pan, H. Xie, Z. Wang, K. Qian, Z. Wang, Study on subset size selection in digital image correlation for speckle patterns, Opt. Express 16 (10) (2008) 7037–7048.
[51] M. Stewart, M.G. Cain, D. Hall, Ferroelectric Hysteresis Measurement & Analysis, Report (no.cmmt/a.152) Issn 1368-6550; ed., National Physical Laboratory and University of Manchester, may (1999).
[52] A.M. Glazer, P. Groves, D.T. Smith, Automatic sampling circuit for ferroelectric hysteresis loops, J. Phys. E 17 (2) (1984) 95–97.
[53] C. Lane, R.L. Burguete, A. Shterenlikht, An objective criterion for the selection of an optimum DIC pattern and subset size, Proceedings of the XIth International Congress and Exposition on Experimental and Applied Mechanics, (2008).
[54] M. Bornert, F. Brémand, P. Doumalin, J.-C. Dupré, M. Fazzini, M. Grédia, F. Hild, S. Mistou, J. Molimard, J.-J. Orteu, et al., Assessment of digital image correlation measurement errors: methodology and results, Exp. Mech. 49 (3) (2009) 353–370, https://doi.org/10.1007/s11340-008-9204-7.
[55] G. Crammond, S.W. Boyd, J.M. Dulieu-Barton, Speckle pattern quality assessment for digital image correlation, Opt. Lasers Eng. 51 (2013) 1368–1378, https://doi.org/10.1016/j.optlaseng.2013.03.014 2013.
[56] S. Roux, F. Hild, Stress intensity factor measurements from digital image correlation: post-processing and integrated approaches, Int. J. Fract. 140 (1-4) (2006) 141–157.
[57] V. Segouin, M. Domenjoud, Y. Bernard, L. Daniel, Development of a 2D DIC experimental tool for piezoelectric strains measurements, International Digital Imaging Correlation Society, (2017), pp. 45–50.
[58] O. Zienkiewicz, R. Taylor, 5th ed., The Finite Element Method: The Basis 1 Butterworth-Heinemann, 2000.
[59] H. Tang, S. Zhang, Y. Feng, F. Li, T.R. Shrout, Piezoelectric property and strain behavior of $Pb(Yb_{0.5}Nb_{0.5})O_3$-$PbHfO_3$-$PbTiO_3$ polycrystalline ceramics, J. Am. Ceram. Soc. 96 (9) (2013) 2857–2863.
[60] Y.A. Genenko, J. Glaum, M.J. Hoffmann, K. Albea, Mechanisms of aging and fatigue in ferroelectrics, Mater. Sci. Eng. B 192 (2015) 52–82.
[61] B. Kaeswurm, V. Segouin, L. Daniel, K.G. Webber, The anhysteretic polarisation of ferroelectrics, J. Phys. D Appl. Phys. 44 (2018) 2358–2363.
[62] T. Morita, T. Ozaki, Magnetic force memory effect using a magnetostrictive material and a shape memory piezoelectric actuator composite, Sens. Actuators A Phys. 161 (2010) 266–270.
[63] C. De, S. Ghara, A. Sundaresan, Effect of internal electric field on ferroelectric polarization in multiferroic $tbmno_3$, Solid State Commun. 205 (2015) 61–65.
[64] S. Sukesha, V. Renu, N. Kumar, Variation of piezoelectric coefficient and dielectric constant with electric field and temperature: a review, Proceedings of 2014 RAECS UIET, (2014).
[65] S. Li, W. Cao, L.E. Cross, The extrinsic nature of nonlinear behavior observed in lead zirconate titanate ferroelectric ceramic, J. Appl. Phys. 69 (1991) 7219.
[66] C.C. Chung, Microstructural Evolution in Lead Zirconate Titanate (Pzt) Piezoelectric Ceramics, Ph.D. dissertation, North Carolina State University, 2014.
[67] D. Damjanovic, M. Demartin, The rayleigh law in piezoelectric ceramics, J. Phys. D Appl. Phys. 29 (7) (1996).